J. Fluid Mech. (2024), *vol*. 986, A14, doi:10.1017/jfm.2024.362

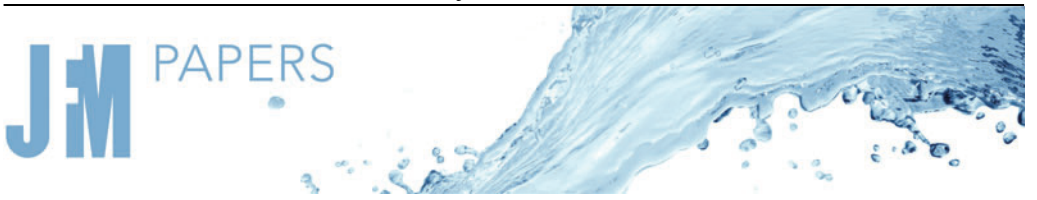

Ciliary propulsion through non-uniform flows

H. Nganguia[1],† **and D. Palaniappan**[2],†

[1]Department of Mathematics, Towson University, Towson, MD 21252, USA

[2]Department of Mathematics and Statistics, Texas A&M University–Corpus Christi, Corpus Christi, TX 78412, USA

(Received 23 October 2023; revised 12 March 2024; accepted 5 April 2024)

The classical paper by Lighthill (*Commun. Pure Appl. Maths*, vol. 109, 1952, p. 118) on the propulsion of ciliated microorganisms has become the reference against which many modern studies on swimming in low Reynolds number are compared. However, Lighthill's study was limited to propulsion in a uniform flow, whereas several biologically relevant microorganisms experience non-uniform flows. Here we propose a benchmark for ciliary propulsion in paraboloidal flows. We first consider the axisymmetric problem, with the microorganisms on the centreline of the background flow, and derive exact analytical solutions for the flow field. Our results reveal flow features, swimming characteristics and performance metrics markedly different from those generated in a uniform flow. In particular, the background paraboloidal flow introduces a Stokes quadrupole singularity at the leading-order flow field, generating vortices. Moreover, we determine the necessary conditions on the strength of the background flow for optimal power dissipation and swimming efficiency. We then consider the more general case of a microorganism off the centreline of the background flow. In this case, the squirmer experiences a paraboloidal, linear shear and uniform flows due to its position relative to the flow's centreline. Our findings show that while the linear shear flow does not affect the translational and rotational velocities of the squirmer, it does influence the velocity field and, therefore, the power dissipation.

Key words: swimming/flying

† Email addresses for correspondence: hnganguia@towson.edu, devanayagam.palaniappan@tamucc.edu

1. Introduction

Fundamental research on microorganisms' swimming in general, and ciliary propulsion in particular, is of great practical importance. It has led to the development of microrobots (Nelson, Kaliakatsos & Abbott 2010; Wu *et al.* 2020) that are employed in a wide range of biological and biomedical applications (Wang *et al.* 2022) such as drug delivery systems (Gao *et al.* 2012; Li *et al.* 2017; Tsang *et al.* 2020; Wu *et al.* 2020; Zhang *et al.* 2021). Lighthill's seminal work on ciliary propulsion in a Newtonian fluid (Lighthill 1952) spearheaded many modern studies on the swimming of ciliated microorganisms. The pioneering study remains the reference to assess the performance metrics of ciliated microorganisms in a variety of environments including heterogeneous media (Leshansky 2009; Nganguia & Pak 2018) and complex fluids (Pak *et al.* 2012; Datt *et al.* 2015; Pietrzyk *et al.* 2019). A common feature between Lighthill and the investigations that followed is the assumption of a background uniform flow. However, many biological systems live in dynamic fluid environments that are subject to non-uniform flows such as small pathogens in blood vessels (Uppaluri *et al.* 2012), spermatozoa swimming through cervical mucus and vaginal fluid (Rutllant, Lopez-Bejar & Lopez-Gatius 2005; Riffell & Zimmer 2007; Zimmer & Riffell 2011; Denissenko *et al.* 2012), among others.

Focusing specifically on Poiseuille flows ubiquitous in the biological microcirculation, experiments dating back to the 1960s have explored its effect on the dynamics of a suspension of particles (Goldsmith & Mason 1961; Segré & Silberberg 1961). Later, Kessler investigated the influence of Poiseuille flows on the directed locomotion of algal cells (Kessler 1985) whereas, much more recently, other investigators have reported Poiseuille flows' effects on the dynamics, orientations and trajectories of biological microorganisms (Zottl & Stark 2012; Choudhary *et al.* 2022; Omori *et al.* 2022; Walker *et al.* 2022), artificial microswimmers (Acemoglu & Yesilyurt 2015) and vesicles (Danker, Vlahovska & Misbah 2009; Agarwal & Biros 2020).

Zottl & Stark (2012) have investigated the influence of a Poiseuille flow on the swinging and tumbling motion of microswimmers in a channel by reducing the problem to a dynamical system for the position and orientation of the swimmer. Using the squirmer model, they found that hydrodynamic interactions between the swimmer and the channel's walls play an important role in stabilising the upstream motion of the swimmer. Notably, they assumed that the swimmer propelled with the velocity $\boldsymbol{v} = (2B_1/3)\boldsymbol{e}$ of a squirmer in a quiescent flow, where $\boldsymbol{e}$ is the swimmer's orientation. The same assumption appears to have been made by Choudhary *et al.* (2022) in their analysis of the effects of inertia on the motion of a channel-confined squirmer in a Poiseuille flow. In this study, they showed that inertia and the type of squirmer (neutral pusher/puller) play a critical role in determining the stability of the squirmer's dynamics. The importance of the orientation and motility of swimmers in Poiseuille flows was brought to light by Omori *et al.* (2022) who, through experiments and simulations, investigated the precise mechanism behind the rheotactic behaviour of the shape-changing *Chlamydomonas reinhardtii*. In their study, the authors assume a time-dependent swimming velocity to account for change in the velocity due to the swimmer's deformation and orientation namely the background flow. To demonstrate the critical role of cell motility on the trajectory and migration of the microorganism, they conduct experiments on motile vs non-motile cells. Their findings revealed that given an initial position off the centreline of the background flow, only motile cells were able to adjust their strokes in order to continuously migrate towards the centreline. The critical role cell motility plays in ciliates' motion was also investigated by Marumo, Yamagishi & Yajima (2021) using three-dimensional tracking experiments of free-swimming *Tetrahymena*. In their study, the authors reported that the non-motile

cells, while rotating along their symmetry axis, remain on a straight path from their initial position.

These studies illustrate the growing interest on the dynamics of swimming microorganisms in Poiseuille flow, focusing on the influence of motility, orientation and shape on the trajectory and motion of the swimmers. However, the assumption of the swimmer propelling at the same velocity it would in a quiescent flow may not hold in a Poiseuille flow, especially since Poiseuille flows introduce hydrodynamic features that significantly affect motions such as vortices (Zottl & Stark 2012). Moreover, existing studies did not provide information on performance metrics that are critical for the design of artificial microswimmers, such as the work done by swimmers locomoting in Poiseuille flows. These observations reveal that a systematic study of the influence of the Poiseuille flow on the propulsion of biological microorganisms, to derive swimming characteristics and performance metrics akin to those obtained for propulsion in uniform flows (Lighthill 1952; Blake 1971), is lacking.

A Poiseuille flow is obtained by superimposing a uniform flow and a paraboloidal flow, so investigating the influence of paraboloidal flows on the propulsion of microorganisms represents the first key step towards a complete understanding of the influence of Poiseuille flows on microorganisms' propulsion. Note that, in terms of singularities commonly identified in hydrodynamic studies, a uniform flow past a sphere consists of a Stokeslet and potential dipole at the sphere's centre (Lamb 1945; Happel & Brenner 1973). On the other hand, for a paraboloidal flow, one needs a Stokeslet, potential dipole, Stokes quadrupole and potential octupole (Chwang & Wu 1975; Palaniappan & Daripa 2000). The effects of uniform flows on microorganisms' propulsion have been disseminated extensively. However, while the influence of paraboloidal flows on spheres (Chwang & Wu 1975) and droplets (Palaniappan & Daripa 2000, 2005) has been studied, to the best of the authors' knowledge its pivotal effects on the performance metrics and swimming characteristics of microorganisms have yet to be explored. The present study addresses this gap in knowledge.

Our paper is organised as follows. We first consider the axisymmetric case in § 2, where the microswimmer is aligned on the centreline of the background flow. After formulating the problem and solving the governing equations, we discuss the various performance metrics including the propulsion speed, power dissipation and swimming efficiency. In § 3 we then analyse the most general case that accounts for the position and orientation of the microswimmer off the centreline of the background flow. Finally, we conclude with few remarks on the implication of our work in § 4.

2. Propulsion along the centreline

We first consider the case of an axisymmetric unbounded paraboloidal flow of strength $\tilde{U}_p$ whose stream function is given by $\tilde{\psi}_\infty = \tilde{U}_p r^4 \sin^4\theta/4$ (Jeong 2019) where the $(\tilde{\ })$ denotes dimensional variables. The corresponding flow field becomes

$$\tilde{\boldsymbol{u}}_\infty = \left\langle \frac{1}{r^2\sin\theta}\frac{\partial\tilde{\psi}_\infty}{\partial\theta}, -\frac{1}{r\sin\theta}\frac{\partial\tilde{\psi}_\infty}{\partial r}\right\rangle = \tilde{U}_p\left\langle r^2\sin^2\cos\theta, -r^2\sin^3\theta\right\rangle. \tag{2.1}$$

The microswimmer is modelled as a squirmer with surface velocity (Lighthill 1952; Blake 1971; Pedley 2016)

$$\tilde{\boldsymbol{u}}_{sq} = \sum_{n=1}^{\infty} A_n P_n(\cos\theta)\boldsymbol{e}_r + \sum_{n=1}^{\infty} B_n V_n(\cos\theta)\boldsymbol{e}_\theta, \tag{2.2}$$

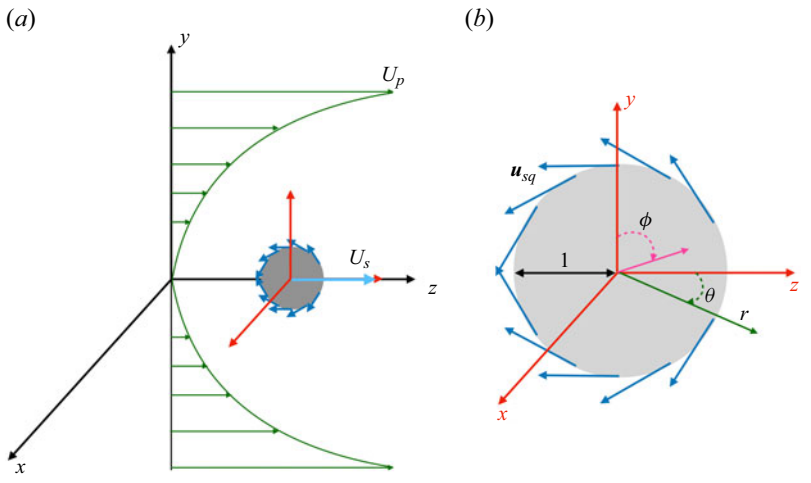

Figure 1. A squirmer with surface velocity $\boldsymbol{u}_{sq}$ propelling with velocity U_s in an unbounded paraboloidal flow with velocity strength U_p. The squirmer is positioned at the centre of the background flow profile, translating along the $\boldsymbol{e}_z$ direction.

where A_n and B_n are the radial and tangential swimming modes, respectively, $P_n(\cos\theta)$ are the Legendre polynomials, $V_n(\cos\theta) = -2/[n(n+1)]P_n^1(\cos\theta)$ and $P_n^1(\cos\theta)$ are the associated Legendre polynomials. The squirmer translates with velocity $\tilde{U}_s$ and is placed at the centreline of the paraboloidal flow (figure 1). Moreover, we consider the problem in the laboratory frame of reference where the origin of the coordinate system is taken to be at the centre of the squirmer with the parabolic flow evaluated at the origin. In this configuration, the squirmer is translating in a fluid that is quiescent in the far-field (Schonberg & Hinch 1989; Asmolov 1999; Hood, Lee & Roper 2015).

All equations governing the problem are scaled using the squirmer's radius a for length, the first swimming mode B_1 for velocity, and the ratio $\mu B_1/a$ for pressure (where μ is the viscosity of the fluid). Note that in the case of a radial squirmer, A_1 is used in place of B_1. Given the size of the microswimmer, inertial effects can be omitted and the flow field is governed by the incompressible Stokes equation

$$-\boldsymbol{\nabla} p + \nabla^2 \boldsymbol{u} = \boldsymbol{0}, \quad \boldsymbol{\nabla}\cdot\boldsymbol{u} = 0, \tag{2.3a,b}$$

where p and $\boldsymbol{u}$ are the pressure and velocity fields of the fluid, respectively. The dimensionless squirmer's surface velocity

$$\boldsymbol{u}_{sq} = \sum_{n=1}^{\infty} \alpha_n P_n(\cos\theta)\boldsymbol{e}_r + \sum_{n=1}^{\infty} \beta_n V_n(\cos\theta)\boldsymbol{e}_\theta. \tag{2.4}$$

For a radial squirmer ($\beta_n = 0$), $\alpha_n = A_n/A_1$ whereas $\beta_n = B_n/B_1$ for a tangential squirmer ($\alpha_n = 0$). Note that the parameters B_1, B_2 and B_3 are associated with a Stokeslet, a stresslet and a Stokes quadrupole, respectively (Pak & Lauga 2014). Physically, the B_1 mode determines the propulsion speed while the B_2 mode dominates the far-field flow induced by the swimmer and, typically, captures the swimmer's typologies (neutral, pusher, puller). For this reason, many previous studies have neglected modes beyond $n = 2$ (Zhu, Lauga & Brandt 2012; Chisholm *et al.* 2016; Li, Lauga & Ardekani 2021; Thery, Maab & Lauga

2023). The velocity field in the far-field is

$$\boldsymbol{u}(r \to \infty) = \boldsymbol{0}, \tag{2.5}$$

and

$$\boldsymbol{u}(r = 1) = \boldsymbol{U}_s + \boldsymbol{u}_{sq} - \boldsymbol{u}_\infty, \tag{2.6}$$

on the surface of the squirmer where, after some algebraic manipulations, the dimensionless spatially varying paraboloidal flow can be expressed in the form

$$\boldsymbol{u}_\infty = U_p \left\langle r^2 \left[\tfrac{2}{5} \left(P_1(\cos\theta) - P_3(\cos\theta) \right) \right], -r^2 \left[\tfrac{2}{15} \left(P_3^1(\cos\theta) - 6P_1^1(\cos\theta) \right) \right] \right\rangle, \tag{2.7}$$

with $U_p = \tilde{U}_p / B_1$ (see Appendix A for details of the derivation). We deduce from (2.7) that the paraboloidal flow will affect the flow field up to order $n = 3$. Thus, while previous studies in uniform flows have justifiably omitted swimming modes $B_{n\geq 3}$, here we consider a three-mode squirmer to fully characterise the effect of paraboloidal flows on swimming.

We use Lamb's general solution for the incompressible Stokes equation (Lamb 1945; Happel & Brenner 1973)

$$u_r = \sum_{n=0}^{\infty} \left(O_n r^{n+1} + Q_n r^{n-1} + \frac{R_n}{r^n} + \frac{S_n}{r^{n+2}} \right) P_n(\cos\theta), \tag{2.8}$$

$$u_\theta = \sum_{n=1}^{\infty} \left(-\frac{n+3}{2} O_n r^{n+1} - \frac{n+1}{2} Q_n r^{n-1} + \frac{n-2}{2} \frac{R_n}{r^n} + \frac{n}{2} \frac{S_n}{r^{n+2}} \right) V_n(\cos\theta) \tag{2.9}$$

and the boundary conditions to determine the exact flow and pressure fields. The coefficients O_n, Q_n, R_n, S_n in the general solution are expressed in terms of the propulsion speed U_s that, in turn, is obtained by applying the force-free condition on the surface of the squirmer S ($r = 1$)

$$\int_S \boldsymbol{\sigma} \cdot \boldsymbol{n} \, \mathrm{d}S = \boldsymbol{0}, \tag{2.10}$$

where $\boldsymbol{\sigma} = -p\boldsymbol{I} + \nabla\boldsymbol{u} + (\nabla\boldsymbol{u})^{\mathrm{T}}$, $\boldsymbol{I}$ is the identity tensor and $\boldsymbol{n} = \boldsymbol{e}_r$ is the unit outward normal vector. In spherical coordinates the swimming direction $\boldsymbol{e}_z = \cos\theta \boldsymbol{e}_r - \sin\theta \boldsymbol{e}_\theta$, and (2.10) reduces to

$$\int_0^{2\pi} \int_0^{\pi} (\sigma_{rr}\cos\theta - \sigma_{r\theta}\sin\theta)|_{r=1} \sin\theta \, \mathrm{d}\theta \, \mathrm{d}\phi = 0. \tag{2.11}$$

After lengthy calculations, (2.11) yields the propulsion speed

$$\tilde{U}_s = \tfrac{1}{3} \left[-A_1 + 2B_1 + 2U_p (A_1 + B_1) \right]. \tag{2.12}$$

Equation (2.12) contrasts with the propulsion speed $\tilde{U}_{uniform} = (2B_1 - A_1)/3$ of a spherical squirmer in a uniform flow (Lighthill 1952; Blake 1971). However, the speed remains independent of higher swimming modes $A_{n\geq 2}$ and $B_{n\geq 2}$. In keeping with previous studies, in the rest of our analysis we only consider the flow field generated by a squirmer with purely tangential surface velocity. The value $U_p = -1$ corresponds to the propulsion-free case, when the background flow is tuned to negate the first swimming mode B_1. This configuration is equivalent to the *pumping* problem (Pak & Lauga 2014), when the squirmer is held fixed and the flow field is generated solely as a result of interaction between the background flow and the surface velocity.

Substituting $U_s = 2(1 + U_p)/3$ and the coefficients O_n, Q_n, R_n, S_n $(n \leq 3)$ into the solutions, the flow field $\boldsymbol{u} = \langle u_r, u_\theta \rangle$ and pressure are obtained as

$$u_r = \frac{2\cos\theta}{3r^3} - \frac{\beta_2\left(r^2-1\right)(3\cos 2\theta + 1)}{4r^4} + \beta_3\left[\frac{\cos\theta(5\cos 2\theta - 1)}{4r^5} - \frac{\cos\theta(5\cos 2\theta - 1)}{4r^3}\right] + U_p\frac{\left[3 - r^2 + 3\left(7r^2 - 5\right)\cos 2\theta\right]}{12r^5}\cos\theta, \tag{2.13}$$

$$u_\theta = \frac{\sin\theta}{3r^3} + \frac{\beta_2\sin\theta\cos\theta}{r^4} - \frac{\beta_3\left(r^2-3\right)\sin\theta(5\cos 2\theta + 3)}{16r^5} + U_p\frac{\left[-27 + 19r^2 + 3\left(7r^2 - 15\right)\cos 2\theta\right]}{48r^5}\sin\theta, \tag{2.14}$$

$$p = \frac{\beta_2(-24r\cos 2\theta - 8r)}{16r^4} + \frac{\beta_3(-15\cos\theta - 25\cos 3\theta)}{16r^4} + U_p\frac{7\,(3\cos\theta + 5\cos 3\theta)}{16r^4}. \tag{2.15}$$

Note that in the absence of a background flow ($U_p = 0$), the velocity field reduces to that of a squirmer in a quiescent fluid (Lighthill 1952; Blake 1971). The velocity field can also be expressed in the form $\boldsymbol{u} = \langle \partial\psi/\partial\theta/(r^2\sin\theta), -\partial\psi/\partial r/(r\sin\theta)\rangle$ where the stream function

$$\psi = \frac{\sin^2\theta}{3r} - \frac{\beta_2\left(r^2-1\right)\sin^2\theta\cos\theta}{2r^2} + \frac{\beta_3\sin^2\theta\left[-15\left(r^2-1\right)\cos 2\theta - 9r^2 + 9\right]}{48r^3} + U_p\frac{\sin^2\theta\left[3\left(7r^2-5\right)\cos 2\theta + 19r^2 - 9\right]}{48r^3}. \tag{2.16}$$

To validate our results, we employed physics-informed neural networks (PINNs) to approximate the velocity field for $U_p = 0$, and the propulsion speed U_s for various values of the background flow's maximum velocity (see Appendix B for details). Recall again that paraboloidal flows only affect the first and third terms in Lamb's general solution. Therefore, for $n = 2$ and $n \geq 4$, the velocity fields generated as a result of squirming in a paraboloidal flow and quiescent fluid are identical.

2.1. *Flow field*

The squirmer propels against the direction of the background flow. Thus, propulsion is along the positive (negative) z direction when the background flow is directed towards the negative (positive) z direction ($U_p < 0$) [($U_p > 0$)]. The flow field informs us on the types of hydrodynamic interactions between squirmers and other organisms/particles one can expect. We consider three cases to analyse the flow fields: $U_p = -2$, $U_p = -1$ (no propulsion) and $U_p = 1$. Figure 2 shows the velocity magnitude and streamlines for a neutral squirmer (figure 2*a–d*) and a pusher with $\beta_2 = -1$ (figure 2*e–h*). In a quiescent flow (figure 2*a*), neutral squirmers generate currents that advect particles in front of the swimmer away from the swimmer, whereas particles on the back of the swimmer are pulled towards the swimmer. This dynamics contrasts with that observed in a paraboloidal flow, as illustrated in figures 2(*b*)–2(*d*). In these cases, the situation is reversed: particles are drawn towards the swimmer at the front and driven away from its back. This behaviour is consistent across magnitudes of the background flow, including in the absence of

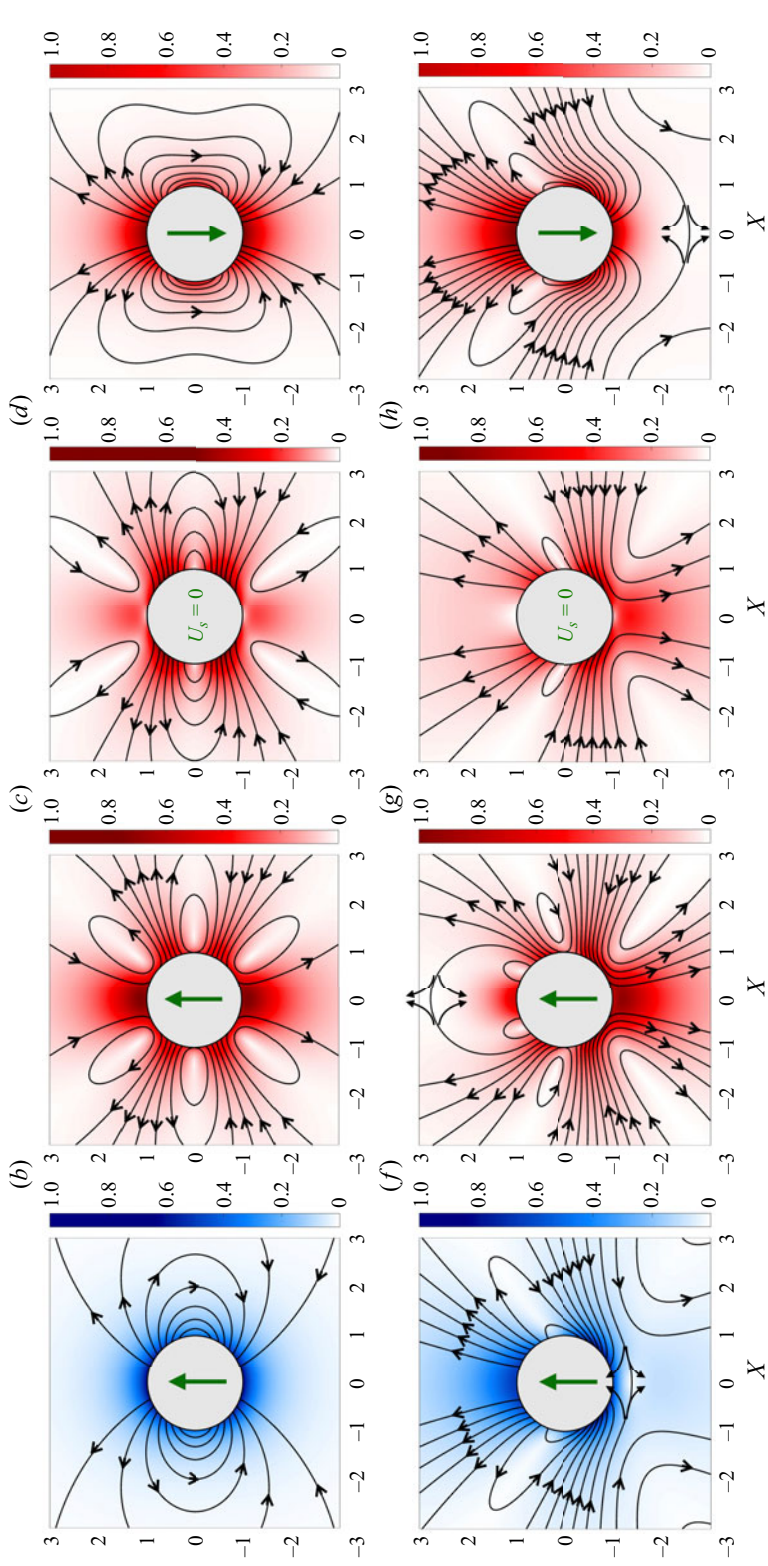

Figure 2. Velocity magnitude and streamlines for (*a–d*) a neutral squirmer ($\beta_2 = 0$, $\beta_3 = 0$) and (*e–h*) a pusher ($\beta_2 = -1$, $\beta_3 = 0$) in a uniform flow (*a*,*e*) and in a paraboloidal flow with $U_p = -2$ (*b*,*f*), $U_p = -1$ (*c*,*g*) and $U_p = 1$ (*d*,*h*). The streamlines extending through the axis of symmetry $x = 0$ in (*e*,*f*,*h*) denote a separatrix: flow is directed towards the swimmer in the vicinity of the latter, and away from the swimmer in the far field. This is represented by the arrows. The colour bar represents the magnitude of the velocity field.

propulsion when the flow cancels out the propulsion generated by the squirmer's surface velocity ($\hat{U}_p = B_1$). For pushers in a quiescent flow (figure 2*e*), particles are advected away from the swimmer both at the front and back, unless they are at the immediate vicinity of the swimmer's back, in which case the particles are pulled towards the swimmer. This overall dynamic is also observed in paraboloidal flows and across magnitudes of the background flow (figure 2*f*–*h*). The flow fields generated by three-mode squirmers show interesting and non-trivial variations that depend on the strength of the third mode β_3. This, in turn, has important implications on the hydrodynamic interactions experienced at the front and back of a three-mode squirmer. Figure 3 shows the velocity magnitude and streamlines for a three-mode squirmer with (figure 3*a*,*b*) $\beta_3 = -1$ and (figure 3*c*–*f*) $\beta_3 = -20$. At $\beta_3 = -1$ in a uniform flow (figure 3*a*,*c*), the interaction dynamics is similar to that of a neutral squirmer: particles are repulsed at the front of the swimmer and attracted at the back. The dynamics is reversed in a paraboloidal flow (figure 3*b*,*d*), where this time particles move towards the swimmer's front whereas they are being advected away from its back. The flow field generated by the squirmer becomes nearly identical in uniform flows compared with paraboloidal flows when the magnitude of the swimming mode is increased. Figures 3(*e*) and 3(*f*) show the microvortices that are generated during the squirmer's motion. Although their features are similar, the velocity fields of the squirmers differ in their orientation. As a result, while the squirmer repels (draws in) particles at their front (back) in a quiescent fluid, it behaves in the opposite manner in a paraboloidal flow by pulling in (advecting away) particles at its front (back).

An interesting feature that also influences hydrodynamic interactions are vortices (or *eddies*). They have been reported for pushers and pullers with rotational velocities near a wall or flat plate (Drescher *et al.* 2009; Poddar, Bandopadhyay & Chakraborty 2020) and in the feeding patterns of starfish (Gilpin, Prakash & Prakash 2017). In unbounded domains, these microvortices appear to be a signature of three-mode squirmers with large β_3 in both uniform flows (see Gilpin *et al.* (2017) and figure 3*e*) and paraboloidal flows (figure 3*f*).

Moreover, while microvortices are not present for three-mode squirmers in quiescent fluids with relatively small β_3, their presence in paraboloidal flows shows a dependence on the strength of the background flow. Specifically, microvortices are only observed for three-mode squirmers with small β_3 and $U_p < 0$, as illustrated in figure 3(*b*). The existence of vortical regions in the flow field of neutral squirmers and pushers present yet another significant difference between propulsion in uniform flows vs paraboloidal flows. Indeed, the microvortices in figure 2(*b*,*c*) for neutral squirmers and figure 2(*f*) for pushers are a direct consequence of the paraboloidal flows. These flows introduce a Stokes quadrupole in the near-field, resulting in flow patterns similar to those generated by three-mode squirmers with small β_3 and $U_p < 0$ (figure 3*b*) or more generally with large β_3 (figure 3*f*). Here we note that the flow field in a uniform flow has zero vorticity, whereas in a paraboloidal flow the vorticity $\boldsymbol{\nabla} \times \boldsymbol{u} \neq \boldsymbol{0}$. We further remark that vortices, like flow reversals, often point to stagnation points $(x^*, z^*) = (r_s \sin\theta, r_s \cos\theta)$ in the flow. For three-mode squirmers with $\beta_2 = 0$, figure 3(*b*,*e*,*f*) indicates that stagnation points exist along the x-axis ($\theta = \pi/2$), where $u_r = 0$. After setting $u_\theta = 0$, the stagnation points are found to depend on the magnitude of the β_3 mode and on the strength of the background flow. The radius r_s is given by

$$r_s = \pm 3\sqrt{\frac{\beta_3 - U_p}{8 + 3\beta_3 - U_p}}, \tag{2.17}$$

and the stagnation points are represented by the $\star$ symbols in figures 3(*b*) and 3(*f*).

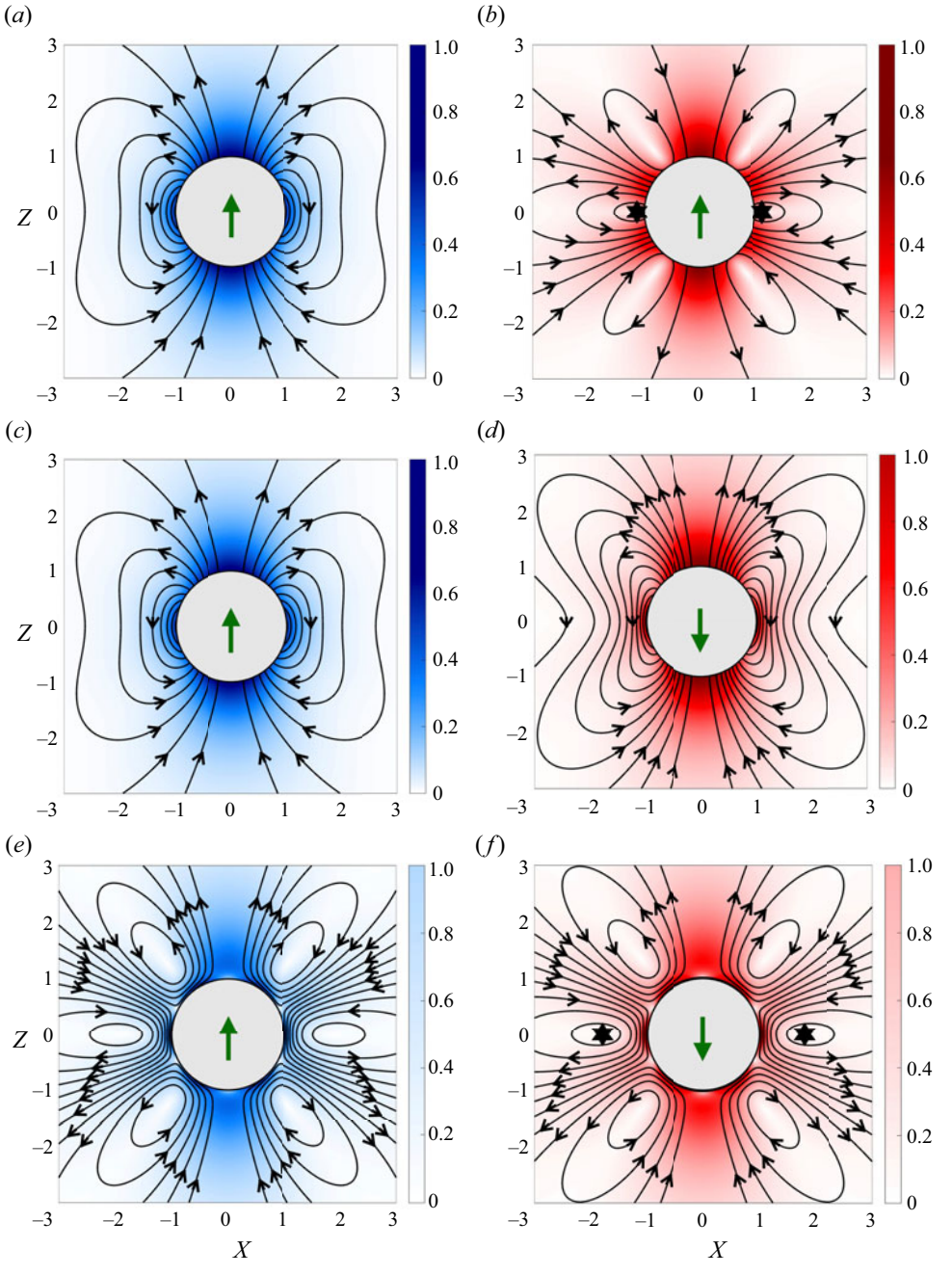

Figure 3. Velocity magnitude and streamlines for a three-mode squirmer with (*a–d*) $\beta_2 = 0, \beta_3 = -1$ and (*e*,*f*) $\beta_2 = 0, \beta_3 = -20$ in a uniform flow (*a*,*c*,*e*) and in a paraboloidal flow with $U_p = -2$ (*b*) and $U_p = 1$ (*d*,*f*). The colour bar represents the magnitude of the velocity field. The ($\star$) symbols on either side of the squirmer in (*b*,*f*) denote the location of stagnation points, given by (2.17).

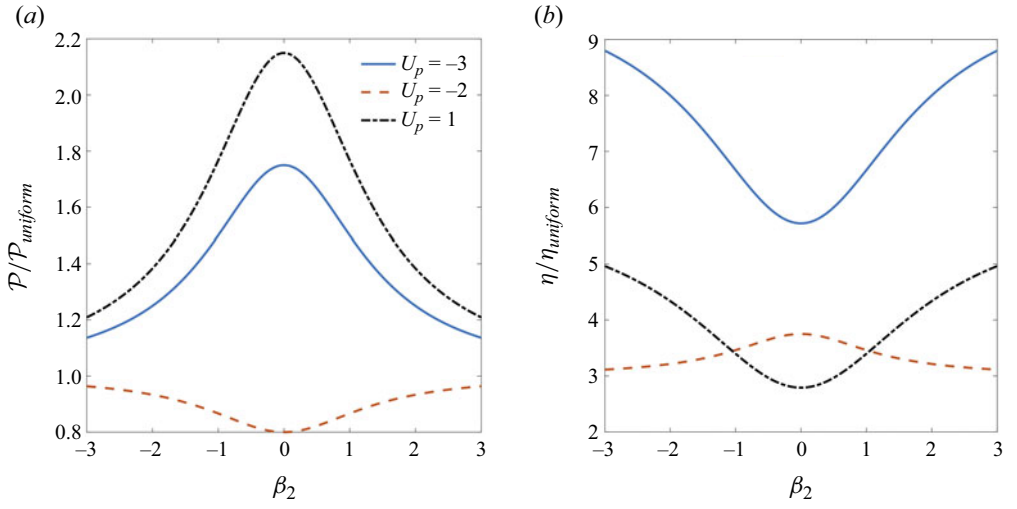

Figure 4. Paraboloidal-to-uniform ratios of (*a*) power dissipation and (*b*) swimming efficiency as a function of the β_2 swimming mode for various strengths of the paraboloidal background flow U_p.

2.2. *Power dissipation and swimming efficiency*

In this section, we discuss the work done by the squirmer and its efficiency. The power dissipation is given by $\mathcal{P} = -\int_S \boldsymbol{\sigma} \cdot \boldsymbol{u} \cdot \boldsymbol{n}\, \mathrm{d}S$. In spherical coordinates, $\mathcal{P}$ is expressed as

$$\mathcal{P} = -\int_0^{2\pi}\int_0^{\pi} \left(\sigma_{rr}u_r + \sigma_{r\theta}u_\theta + \sigma_{r\phi}u_\phi\right)\big|_{r=1} \sin\theta \,\mathrm{d}\theta \,\mathrm{d}\phi. \tag{2.18}$$

Note that for the axisymmetric motion considered here, $\sigma_{r\phi} = 0$, $u_\phi = 0$. After some calculations, we obtain

$$\mathcal{P} = \frac{4\pi}{105}\left\{70\left(2+\beta_2^2\right) + 35\beta_3^2 - U_p\left[38\beta_3 - 7(16+7U_p)\right]\right\}. \tag{2.19}$$

Equation (2.19) contrasts with the power dissipation $\mathcal{P}_{uniform} = 8\pi(2+\beta_2^2+\beta_3^2/2)/3$ of a squirmer in a uniform flow (Lighthill 1952; Blake 1971). Moreover, we observe that the power dissipation varies not only as a function of the swimming modes, but also as a function of the background flow's strength. For a neutral squirmer ($\beta_2 = \beta_3 = 0$) with $U_p = 0$, we recover $\mathcal{P}_{uniform} = 16\pi/3$. When $U_p < -16/7$ or $U_p > 0$, a neutral squirmer in a paraboloidal flow expends more energy compared with its counterpart in a uniform flow. However, swimming in a paraboloidal flow becomes more beneficial for the squirmer provided $U_p \in (-16/7, 0)$. We can similarly compare the power dissipation for pushers/pullers ($\beta_3 = 0$) in paraboloidal flows relative to their work in uniform flows. Figure 4(*a*) shows the paraboloidal-to-uniform ratio $\varepsilon = \mathcal{P}/\mathcal{P}_{uniform}$ for a range of β_2 values with flow strength $U_p = -3$ (solid), $U_p = -2$ (dashed) and $U_p = 1$ (dash-dotted). As expected from the analysis of the neutral squirmer, pushers/pullers always expend less energy compared with their counterparts in uniform flows for $U_p = -2$.

Before discussing three-mode squirmers, we analyse the efficiency for two-mode squirmers. The swimming efficiency $\eta = F_D U_s/\mathcal{P}$ (Lighthill 1952), where $F_D = F_D^p + F_D^s = 4\pi U_p + 6\pi U_s$ is the force required to drag a rigid sphere at the swimming speed in the same fluid medium. Here, F_D^p alone is the drag force experienced by a rigid sphere in

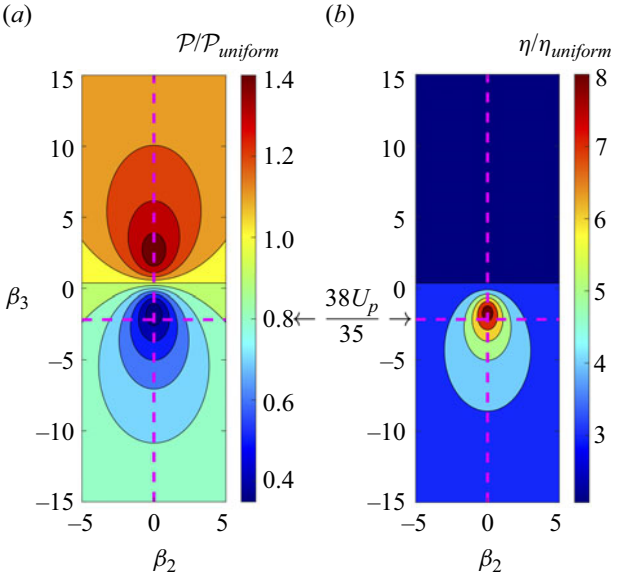

Figure 5. Parameter space of (β_2, β_3) for the paraboloidal-to-uniform ratios of power dissipation (a) and efficiency (b) for a three-mode squirmer with $U_p = -2$. The intersection of the vertical lines correspond to the combination (β_2, β_3) at which a two-mode squirmer in a paraboloidal is a more ideal swimmer than a three-mode squirmer in a uniform flow.

a paraboloidal flow (Chwang & Wu 1975) while F_D^s is the Stokes drag in the absence of a paraboloidal background flow. After some simplification, the efficiency is given by

$$\eta = \frac{70(1+U_p)(1+2U_p)}{70\left(2+\beta_2^2\right)+35\beta_3^2-U_p\left[38\beta_3-7(16+7U_p)\right]}. \tag{2.20}$$

Figure 4(b) shows the ratio $\nu = \eta/\eta_{uniform}$ for the flow strengths in figure 4(a). In this case, the efficiency of a swimmer in a uniform flow is given by $\eta_{uniform} = 1/(2+\beta_2^2+\beta_3^2/2)$ (Lighthill 1952; Blake 1971). We conclude from the results that all two-mode squirmers in paraboloidal flows experience a gain in swimming efficiency ($\nu > 1$), except for $U_p = -1/2, -1$. For $U_p = -1$ the efficiency is zero since the squirmer does not propel ($U_s = 0$). On the other hand, efficiency is also zero when $U_p = -1/2$ (the drag forces F_D^p and F_D^s cancel each other out).

In the case of a three-mode squirmer, we produce the $\beta_2 - \beta_3$ parameter space (figure 5) to determine the conditions under which the addition of the third swimming mode may yield behaviour distinct from that of a two-mode squirmer. In this analysis, we consider $U_p = -2$. On one hand, figure 5(a) shows that squirmers in a paraboloidal flow expend more energy when $\beta_3 \gtrapprox 0.5$. On the other hand, while the ratio ε may vary depending on β_3, figure 5(b) shows that $\nu > 1$ for a three-mode squirmer. Thus, despite ε being greater than unity, the three-mode squirmer is always a more efficient swimmer in paraboloidal flows compared with uniform flows.

The parameter spaces in figure 5 are subdivided into distinct spheroidal-shaped 'holes' or 'sinks', especially in the regions $\beta_3 < 0.5$ for the swimming efficiency (figure 5b). The smallest of these sinks $\mathcal{S}$ contains the combinations (β_2, β_3) that minimise power dissipation and maximise swimming efficiency. The location of the epicentre of $\mathcal{S}$ is $(0, 38U_p/35)$, as illustrated by the intersection of the dashed lines in figure 5. The case

$\beta_3 = 38U_p/35$ corresponds to the non-zero value that eliminates the expression $35\beta_3^2 - 38U_p\beta_3$ in (2.19) and (2.20). In other words, at this value a three-mode squirmer in a paraboloidal flow expends the same energy and swims as efficiently as a two-mode squirmer subject to the same background flow. This suggests that squirmers in paraboloidal flows may be able to take advantage of the background flow to lower their rate of work and become more efficient swimmers. In terms of artificial microswimmers, our findings raise the possibility of novel design principles for microrobots that take advantage of specific properties of the background flow to reduce their work.

To conclude this section, we discuss the potential biological relevance of these results. The first swimming mode B_1 can be approximated using $B_1 = 3\tilde{U}_s/2$ where $\tilde{U}_s$ is obtained from experimental measurements of the velocity of various microorganisms including ciliates (Rodrigues, Lisicki & Lauga 2021). Values of the $\beta_2 = B_2/B_1$ swimming modes have been estimated previously for artificial and biological swimmers (Evans *et al.* 2011). In general, they range from -1 (*Escherichia coli* Drescher *et al.* 2011), to ≈ 0 (*Volvox* Short *et al.* (2006) and artificially created squirmers such as autonomous vesicles Miura *et al.* (2010) or squirming droplets Thutupalli, Seemann & Herminghaus 2011), to 1 (*Chlamydomonas* Pedley & Kessler 1990). This range of β_2 values lies squarely in the region of least power expenditure and greatest efficiency found in figure 5. Biological microorganisms naturally strive to optimise their motion, and our results capture this behaviour. To the best of the authors' knowledge, measurements of higher swimming modes have not been performed on biological microorganisms. Moreover, higher modes lead to greater energy expenditure and less efficient swimming. Our results, however, raise the possibility of designing still-efficient artificial microswimmers. Specifically, the later can be built by accounting for the properties of the background flow such that adding a third swimming mode with $B_3 \approx \tilde{U}_p$ does not increase (decrease) the power dissipation (swimming efficiency) of the microswimmer compared with a swimmer with only the first two modes. In addition to minimising work, the carefully added swimming gait could serve other purposes such as aiding in the transport of cargo (Ouyang *et al.* 2023).

3. A note on the propulsion of an off-centred squirmer

Results presented in § 2 apply to the propulsion of a squirmer located on the centreline of the paraboloidal flow, in which case the swimmer can only propel along the background flow direction $\boldsymbol{e}_z$. For completeness, we now consider the case of a squirmer that is positioned off the centreline of the background flow. The latter is located at a distance (x_0, y_0) from the origin (figure 6). We specifically focus on determining the translational and rotational velocities of the squirmer in this general case.

The paraboloidal flow in Cartesian coordinates is given by (Chwang & Wu 1975)

$$\tilde{\boldsymbol{u}}_\infty = \bar{U}_p \left[(x - x_0)^2 + (y - y_0)^2 \right] \boldsymbol{e}_z. \tag{3.1}$$

Expanding the quadrating terms and simplifying yields the paraboloidal flow in spherical coordinates

$$\tilde{\boldsymbol{u}}_\infty = \bar{U}_p \left[r^2 \sin^2\theta - r\sin\theta\,(\dot{\gamma}_1 \cos\phi + \dot{\gamma}_2 \sin\phi) + \Gamma \right] \boldsymbol{e}_z, \tag{3.2}$$

where $\dot{\gamma}_1 = 2x_0$ and $\dot{\gamma}_2 = 2y_0$ are local shear rates and $\Gamma = x_0^2 + y_0^2$. Equation (3.2) reveals that in addition to the paraboloidal flow $\bar{U}_p r^2 \sin^2\theta \boldsymbol{e}_z$, the off-centred squirmer experiences a linear shear flow $-\bar{U}_p r \sin\theta(\dot{\gamma}_1 \cos\phi + \dot{\gamma}_1 \sin\phi)\boldsymbol{e}_z$ and a uniform flow

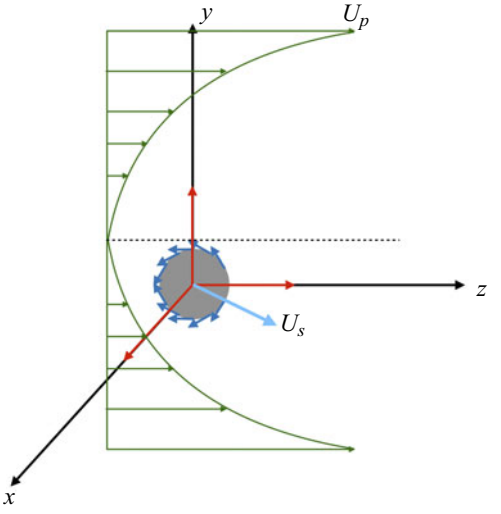

Figure 6. A squirmer with radius a and surface velocity $\boldsymbol{u}_{sq}$ off the centreline of a paraboloidal flow located a distance (x_0, y_0) from the origin.

$\bar{U}_p \Gamma \boldsymbol{e}_z$ (Chwang & Wu 1975; Hanna & Vlahovska 2010). We observe immediately that positioning the squirmer off the centreline of the background flow introduces a rotational motion in the azimuthal direction $\boldsymbol{e}_\phi$ that results from the linear shear flow. The boundary conditions in the laboratory frame become

$$\hat{\boldsymbol{u}}(r = a) = \hat{\boldsymbol{u}}_{sq} + \hat{\boldsymbol{U}}_s + \hat{\boldsymbol{\Omega}}_s \times \boldsymbol{x}_s - \tilde{\boldsymbol{u}}_\infty, \tag{3.3}$$

$$\hat{\boldsymbol{u}}(r \to \infty) = \boldsymbol{0}, \tag{3.4}$$

where $\boldsymbol{x}_s = a\boldsymbol{e}_r$ and $\hat{\boldsymbol{\Omega}}_s = \hat{\Omega}_s \boldsymbol{e}_k$ is the rotational velocity of the squirmer obtained by imposing the torque-free condition

$$\int_S \boldsymbol{x}_s \times (\boldsymbol{\sigma} \cdot \boldsymbol{n})\, \mathrm{d}S = \boldsymbol{0}. \tag{3.5}$$

As in § 2, the translational velocity $\hat{\boldsymbol{U}}_s = \hat{U}_s \boldsymbol{e}_k$ is obtained using the force-free condition (2.10). The index k denotes the coordinates x, y, z, so the translational and rotational velocities can occur in any direction. The generalised surface velocity $\hat{\boldsymbol{u}}_{sq}$ for the purely tangential squirming motion is given by (Pak & Lauga 2014)

$$u_{sq,r} = 0 \tag{3.6}$$

$$u_{sq,\theta} = \sum_{n=1}^{\infty} \sum_{m=0}^{n} \left[-\frac{2 \sin\theta P_n^{m'}}{n a^{n+2}} \left(B_{mn} \cos m\phi + \hat{B}_{mn} \sin m\phi \right) + \frac{m P_n^m}{a^{n+1} \sin\theta} \left(\hat{C}_{mn} \cos m\phi - C_{mn} \sin m\phi \right) \right] \tag{3.7}$$

$$u_{sq,\phi} = \sum_{n=1}^{\infty} \sum_{m=0}^{n} \left[\frac{2m P_n^m}{n a^{n+2} \sin\theta} \left(\hat{B}_{mn} \cos m\phi - B_{mn} \sin m\phi \right) + \frac{\sin\theta P_n^{m'}}{a^{n+1}} \left(C_{mn} \cos m\phi + \hat{C}_{mn} \sin m\phi \right) \right], \tag{3.8}$$

where $P_n^m = P_n^m(\cos\theta)$ are the associated Legendre polynomials and B_{mn}, $\hat{B}_{mn}$, C_{mn} and $\hat{C}_{mn}$ are the squirming modes.

We use Lamb's general solution for exterior problems (Pak & Lauga 2014) and apply the boundary conditions to obtain the velocity field $\boldsymbol{u} = \langle u_r, u_\theta, u_\phi \rangle$ for the general squirming motion of a three-mode squirmer (up to squirming modes B_{03} and C_{03}) in paraboloidal flows. The components of the velocity field are given by (C5)–(C7) in Appendix C. After applying the force- and torque-free conditions ((2.10) and (3.5)), lengthy calculations yield the translational and rotational velocities

$$U_s = \frac{4}{3a^3}\left(B_{11}\boldsymbol{e}_x + \hat{B}_{11}\boldsymbol{e}_y - B_{01}\boldsymbol{e}_z\right) + \bar{U}_p\left(\frac{2}{3}a^2 + \Gamma\right)\boldsymbol{e}_z, \tag{3.9}$$

$$\Omega_s = \frac{1}{a^3}\left(C_{11}\boldsymbol{e}_x + \hat{C}_{11}\boldsymbol{e}_y - C_{01}\boldsymbol{e}_z\right). \tag{3.10}$$

The translational velocity due to purely tangential surface velocity in (2.12) is recovered by using a simple rescaling $B_{01} = -a^3 B_1/2$, $\bar{U}_p = U_p/a^2$ and setting $\Gamma = 0, B_{11} = \hat{B}_{11} = 0$. Moreover, in the absence of a paraboloidal flow ($\bar{U}_p = 0$) the translational and rotational velocities agree with the results obtained using the reciprocal theorem (Pak & Lauga 2014). Note that the propulsion of the off-centred squirmer becomes restricted to the $x-y$ plane when the strength of the paraboloidal flow $\bar{U}_p = 4B_{01}/a^3(2a^2 + 3\Gamma)$.

The power dissipation is calculated using (2.18), and can be expressed in terms of contributions from the quiescent and background flows: $\mathcal{P} = \mathcal{P}_{uniform} + \mathcal{P}_{\bar{U}_p}$. In this case, $\mathcal{P}_{uniform}$ is the expression obtained by Pak & Lauga (2014) for a non-axisymmetric squirmer (equation (77) in their paper) whereas $\mathcal{P}_{\bar{U}_p}$ is given by

$$\mathcal{P}_{\bar{U}_p} = \pi\mu\left\{-\frac{4}{105}\left[224B_{01} + \frac{72}{a^2}B_{03} - \frac{252}{a^2}\left(\dot{\gamma}_1 B_{12} + \dot{\gamma}_2\hat{B}_{12}\right)\right]\bar{U}_p + \frac{4a^3}{105}\left[41a^2 + 42\left(\dot{\gamma}_1^2 + \dot{\gamma}_2^2\right)\right]\bar{U}_p^2\right\}. \tag{3.11}$$

Equation (3.11) shows that the power dissipation depends explicitly on the linear shear flow, generated as a result of the position of the squirmer relative to the paraboloidal flow's centreline. This result contrasts with (3.9) and (3.10) that do not depend on the local shear rates $\dot{\gamma}_1$ or $\dot{\gamma}_2$, and suggest that the linear shear flow does not influence the translational and rotational velocities of the squirmer. In terms of the dependence on shear flow, our conclusion about the translational velocity is akin to the result obtained by Pak, Feng & Stone (2014) in the case of a surfactant-covered drop in a Poiseuille flow.

4. Concluding remarks

In this paper, we have investigated the propulsion of a spherical ciliated microorganism, represented by a squirmer, in a paraboloidal flow. First, we considered the axisymmetric problem. We have obtained exact analytical solutions of the propulsion speed, power dissipation, swimming efficiency, flow and pressure fields, and contrasted our results with those of Lighthill, the long-standing benchmark for microswimming studies in uniform flows. We have found that while the propulsion speed $U_s = 2(1 + U_p)/3$ only depends on the first swimming mode (as it does for propulsion in uniform flows first reported by Lighthill 1952; Blake 1971), it is now influenced by the strength of the background flow. The dependence on the maximum velocity of the paraboloidal flow played a significant

role in the amount of work being experienced by the squirmer. However, although we have determined the range of flow strength that minimises work, we have shown that squirmers in paraboloidal flows are always more efficient compared with squirmers in uniform flows. We then considered the more general, non-axisymmetric problem of a squirmer off the centreline of the background flow. In this framework, the shear-induced orientation and rotation of the squirmer now enter the problem. We have determined that the translational and rotational velocities of the squirmer are independent of the linear shear flow induced by the background flow. However, the linear shear-flow plays a role in the velocity field generated by the squirmer.

Since paraboloidal flows are a critical component of Poiseuille flow, our findings provide metrics for future studies of microswimming in this biologically relevant non-uniform flow. Specifically, critical questions to be addressed include: How will propulsion in complex fluids compare with locomotion in Newtonian fluids? What gains in performance metrics will particle geometry yield compared with spherical swimmers? How will swimming with a cage (Reigh & Lauga 2017; Reigh *et al.* 2017) be affected in a paraboloidal flow? Our results also have significant implications on various biological processes that depend on the flow fields generated by microswimmers, including feeding (Magar, Goto & Pedley 2003; Ishikawa *et al.* 2016; Gilpin *et al.* 2017) and hydrodynamic interactions (Jabbarzadeh & Fu 2018).

Funding. H.N. gratefully acknowledges funding support from the National Science Foundation grant no. 2211633, and from a Jess and Mildred Fisher Endowed Professor of Mathematics from the Fisher College of Science and Mathematics at Towson University. H.N. and D.P. thank the anonymous reviewers who provided pertinent suggestions and comments on our submission.

Declaration of interests. The authors report no conflict of interest.

Author ORCIDs.
H. Nganguia https://orcid.org/0000-0002-2107-2754.

Appendix A. Paraboloidal background flow

Here we outline the derivation of the paraboloidal background flow in (2.7). Using the stream function formulation $\psi_\infty = U_p r^4 \sin^4\theta/4$, the background velocity is given by

$$\tilde{\boldsymbol{u}}_\infty = \left\langle U_p r^2 \cos\theta \sin^2\theta, -U_p r^2 \sin^3\theta \right\rangle. \tag{A1}$$

The Legendre and associated Legendre polynomials

$$\left.\begin{aligned} P_1 &= \cos\theta, \\ P_2 &= \tfrac{1}{2}\left(3\cos^2\theta - 1\right), \\ P_3 &= \tfrac{1}{2}\left(5\cos^3\theta - 3\cos\theta\right), \\ P_1^1 &= -\sin\theta, \\ P_2^1 &= -3\cos\theta\sin\theta, \\ P_3^1 &= -6\sin\theta + \tfrac{15}{2}\sin^3\theta, \\ P_2^2 &= 3\sin^2\theta. \end{aligned}\right\} \tag{A2}$$

After some algebraic manipulations, P_3 is used to obtain $\cos\theta \sin^2\theta = 2(P_1 - P_3)/5$. Similarly, P_3^1 is used to obtain $\sin^3\theta = 2(P_3^1 - 6P_1^1)/15$. Substituting $\cos\theta \sin^2\theta$ and $\sin^3\theta$ into (A1) yields

$$\boldsymbol{u}_\infty = U_p \left\langle r^2 \left[\tfrac{2}{5} \left(P_1(\cos\theta) - P_3(\cos\theta) \right) \right], -r^2 \left[\tfrac{2}{15} \left(P_3^1(\cos\theta) - 6P_1^1(\cos\theta) \right) \right] \right\rangle. \quad \text{(A3)}$$

For completeness, we provide the derivatives of the Legendre and associated Legendre polynomials. Note that the derivatives are obtained with respect x, where $P_n^m \equiv P_n^m(x)$, followed by the substitution $x = \cos\theta$:

$$\left.\begin{aligned} P_1' &= 1, \\ P_2' &= 3\cos\theta, \\ P_3' &= \tfrac{3}{2}\left(5\cos^2\theta - 1\right), \\ P_1^{1'} &= \frac{\cos\theta}{\sin\theta}, \\ P_2^{1'} &= \frac{3\cos^2\theta}{\sin\theta} - 3\sin\theta, \\ P_2^{2'} &= -6\cos\theta. \end{aligned}\right\} \quad \text{(A4)}$$

Appendix B. Validation using PINNs

To validate our analytical results, we simulate the propulsion of a pusher with $\beta_2 = -1$ using a PINN. The problem is implemented in DeepXDE (a Python library for scientific machine learning Lu *et al.* 2021) with a Tensorflow backend (Abadi *et al.* 2015). We employ a feed-forward neural network consisting of an input layer with two nodes, three hidden layers with 100 nodes per layer and an output layer with three nodes. We use the Adam optimiser and the hyperbolic tangent as the activation function. The learning rate is gradually lowered using a learning rate scheduler, from an initial value of $\nu = 3 \times 10^{-3}$. A total of 1000 and 300 training points were used inside the computational domain and on the domain's boundaries, respectively. We perform the computations in the domain $[r, \theta] = [1, 10] \times [0, \pi]$. Figure 7 shows comparisons of the velocity magnitude $\|\boldsymbol{u}\| = \sqrt{u_r^2 + u_\theta^2}$ as a function of the radius for the flow in the back ($\theta = \pi$, figure 7*a*) and side ($\theta = \pi/2$, figure 7*b*) of a pusher ($\beta_2 = -1$). In both panels, the simulations show good agreement with the analytical solution. The convergence of the PINN simulations towards the propulsion speed is shown in figure 7(*c*) as a function of the number of iterations for various values of the strength of the background paraboloidal flow.

Appendix C. Derivation of the coefficients in the velocity field

Here we provide an outline of the derivation of the coefficients in the velocity field of the general squirming motion. Lamb's general solution for three-dimensional exterior

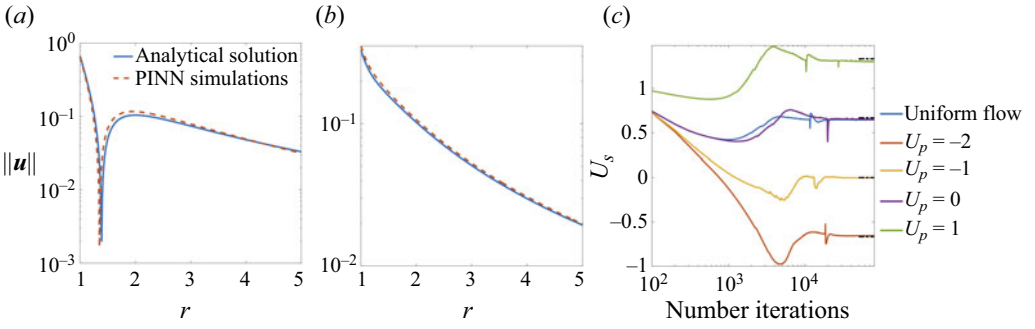

Figure 7. (*a*,*b*) Magnitude of the axisymmetric velocity $\|\boldsymbol{u}\| = \sqrt{u_r^2 + u_\theta^2}$ as a function of the radius r for a pusher with $\beta_2 = -1$. The flow decay is shown at the back of the squirmer $\theta = \pi$ (*a*) and at the side of the swimmer $\theta = \pi/2$ (*b*). In (*c*), the convergence of the propulsion speed predicted by the PINN simulations is shown as a function of the number of iterations. The curves are colour-coded to denote different values of the paraboloidal flow's strength U_p. The dash-dotted horizontal lines represent the value of the exact propulsion speed, obtained from (2.12).

problems, which satisfies (3.4), is given by (Pak & Lauga 2014)

$$u_r = \sum_{n=1}^{\infty}\sum_{m=0}^{n} \frac{(n+1)P_n^m}{2(2n-1)\mu r^{n+2}} \left\{\left[D_{mn}r^2 - 2E_{mn}(2n-1)\mu\right]\cos m\phi + \left[\hat{D}_{mn}r^2 - 2\hat{E}_{mn}(2n-1)\mu\right]\sin m\phi\right\} \tag{C1}$$

$$u_\theta = \sum_{n=1}^{\infty}\sum_{m=0}^{n} \frac{1}{2r^n \sin\theta} \left\{\sin^2\theta P_n^{m'}\left[\frac{n-2}{n(2n-1)\mu}\left(D_{mn}\cos m\phi + \hat{D}_{mn}\sin m\phi\right) - \frac{2}{r^2}\left(E_{mn}\cos m\phi + \hat{E}_{mn}\sin m\phi\right)\right] + \frac{2m}{r}P_n^m\left(\hat{F}_{mn}\cos m\phi - F_{mn}\sin m\phi\right)\right\} \tag{C2}$$

$$u_\phi = \sum_{n=1}^{\infty}\sum_{m=0}^{n} \frac{1}{2r^n \sin\theta} \left\{mP_n^m\left[\frac{n-2}{n(2n-1)\mu}\left(-\hat{D}_{mn}\cos m\phi + D_{mn}\sin m\phi\right) - \frac{2}{r^2}\left(-\hat{E}_{mn}\cos m\phi + E_{mn}\sin m\phi\right)\right] + \frac{2}{r}\sin^2\theta P_n^{m'}\left(F_{mn}\cos m\phi + \hat{F}_{mn}\sin m\phi\right)\right\}. \tag{C3}$$

Translation and rotation can occur in any of the $\boldsymbol{e}_x$, $\boldsymbol{e}_y$ and $\boldsymbol{e}_z$, where

$$\left.\begin{aligned} \boldsymbol{e}_x &= \sin\theta\cos\phi\boldsymbol{e}_r + \cos\theta\cos\phi\boldsymbol{e}_\theta - \sin\phi\boldsymbol{e}_\phi, \\ \boldsymbol{e}_y &= \sin\theta\sin\phi\boldsymbol{e}_r + \cos\theta\sin\phi\boldsymbol{e}_\theta + \cos\phi\boldsymbol{e}_\phi, \\ \boldsymbol{e}_z &= \cos\theta\boldsymbol{e}_r - \sin\theta\boldsymbol{e}_\theta. \end{aligned}\right\} \tag{C4}$$

These unit vectors suggest that the velocity fields in these directions will differ only for indices $mn = 01$, 11 whereas the linear shear flow involves index 12. The corresponding

flow field and pressure for a three-mode squirmer are given by

$$
\begin{aligned}
u_r = {} & \frac{1}{\mu r^3}\left\{P_1\left(D_{01}r^2 - 2E_{01}\mu\right)\right. \\
& + P_1^1\left[\left(D_{11}r^2 - 2E_{11}\mu\right)\cos\phi + \left(\hat{D}_{11}r^2 - 2\hat{E}_{11}\mu\right)\sin\phi\right]\Big\} \\
& + \frac{1}{2\mu r^4}\left\{P_2\left(D_{02}r^2 - 6E_{02}\mu\right)\right. \\
& + P_2^1\left[\left(D_{12}r^2 - 6E_{12}\mu\right)\cos\phi + \left(\hat{D}_{12}r^2 - 6\hat{E}_{12}\mu\right)\sin\phi\right] \\
& + P_2^2\left[\left(D_{22}r^2 - 6E_{22}\mu\right)\cos 2\phi + \left(\hat{D}_{22}r^2 - 6\hat{E}_{22}\mu\right)\sin 2\phi\right]\Big\} \\
& + \frac{2}{5\mu r^5}P_3\left(D_{03}r^2 - 10E_{03}\mu\right), \qquad \text{(C5)}
\end{aligned}
$$

$$
\begin{aligned}
u_\theta = {} & \frac{1}{2r\sin\theta}\left\{\sin^2\theta P_1'\left(-\frac{1}{\mu}D_{01} - \frac{2}{r^2}E_{01}\right)\right. \\
& + \sin^2\theta P_1^{1'}\left[-\frac{1}{\mu}\left(D_{11}\cos\phi + \hat{D}_{11}\sin\phi\right) - \frac{2}{r^2}\left(E_{11}\cos\phi + \hat{E}_{11}\sin\phi\right)\right] \\
& \left. + \frac{2}{r}P_1^1\left(\hat{F}_{11}\cos\phi - F_{11}\sin\phi\right)\right\} + \frac{1}{2r^2\sin\theta}\left\{-\frac{2\sin^2\theta P_2'}{r^2}E_{02}\right. \\
& - \frac{2\sin^2\theta P_2^{1'}}{r^2}\left(E_{12}\cos\phi + \hat{E}_{12}\sin\phi\right) + \frac{2}{r}P_2^1\left(\hat{F}_{12}\cos\phi - F_{12}\sin\phi\right) \\
& \left. - \frac{2\sin^2\theta P_2^{2'}}{r^2}\left(E_{22}\cos 2\phi + \hat{E}_{22}\sin 2\phi\right) + \frac{4}{r}P_2^2\left(\hat{F}_{22}\cos 2\phi - F_{22}\sin 2\phi\right)\right\} \\
& + \frac{1}{2r^3\sin\theta}\sin^2\theta P_3'\left(\frac{1}{15\mu}D_{03} - \frac{2}{r^2}E_{03}\right), \qquad \text{(C6)}
\end{aligned}
$$

$$
\begin{aligned}
u_\phi = {} & \frac{1}{2r\sin\theta}\left\{\frac{2\sin^2\theta P_1'}{r}F_{01}\right. \\
& + P_1^1\left[-\frac{1}{\mu}\left(-\hat{D}_{11}\cos\phi + D_{11}\sin\phi\right) - \frac{2}{r^2}\left(-\hat{E}_{11}\cos\phi + E_{11}\sin\phi\right)\right] \\
& \left. + \frac{2\sin^2\theta P_1^{1'}}{r^2}\left(F_{11}\cos\phi + \hat{F}_{11}\sin\phi\right)\right\} + \frac{1}{2r^2\sin\theta}\left\{\frac{2\sin^2\theta P_2'}{r}F_{02}\right. \\
& - \frac{2P_2^1}{r^2}\left(-\hat{E}_{12}\cos\phi + E_{12}\sin\phi\right) + \frac{2\sin^2\theta P_2^{1'}}{r}\left(F_{12}\cos\phi + \hat{F}_{12}\sin\phi\right) \\
& \left. - \frac{4P_2^2}{r^2}\left(-\hat{E}_{22}\cos 2\phi + E_{22}\sin 2\phi\right) + \frac{2\sin^2\theta P_2^{2'}}{r}\left(F_{22}\cos 2\phi + \hat{F}_{22}\sin 2\phi\right)\right\} \\
& + \frac{1}{2r^3\sin\theta}\frac{2\sin^2\theta P_3'}{r}F_{03}, \qquad \text{(C7)}
\end{aligned}
$$

Coefficients	$\boldsymbol{e}_x$	$\boldsymbol{e}_y$	$\boldsymbol{e}_z$
D_{01}	$\triangledown$	$\triangledown$	$\triangledown^*$
D_{02}	$\dfrac{6\mu}{a^2}E_{02}$	–	–
D_{03}	$\mu\left(a^5\bar{U}_p+\dfrac{10}{a^2}E_{03}\right)$	–	–
E_{01}	$\triangle$	$\triangle$	$\triangle^*$
E_{02}	B_{02}	–	–
E_{03}	$\dfrac{a^7}{20}\bar{U}_p+B_{03}$	–	–
F_{01}	C_{01}	C_{01}	$C_{01}+a^3\Omega_s$
F_{02}	C_{02}	–	–
F_{03}	C_{03}	–	–

Table 1. Coefficients of the flow field for $m=0$. The – denotes a coefficient that remains the same across directions. The coefficients represented by $\triangledown$, ∇^*, $\triangle$, $\triangle^*$ are expressed in terms of the translational velocity and/or maximum velocity of the background flow ((C9)–(C11*a*,*b*)).

and

$$\begin{aligned}p=\frac{1}{8\mu r^5}\Big\{&r\cot\theta\left(\sin\theta\left(8D_{01}r^2+3D_{03}\right)-2\cos\phi(3D_{12}r+4\hat{F}_{11}\mu(2r-1))\right.\\&\left.-2\sin\phi(3\hat{D}_{12}r+4F_{11}\mu-8F_{11}\mu r)\right)+r\,(6D_{02}r\cos2\theta\\&+\cos3\theta\csc\theta(5D_{03}\sin\theta+6D_{12}r\cos\phi+6\hat{D}_{12}r\sin\phi\\&-8F_{11}\mu\sin\phi+8\hat{F}_{11}\mu\cos\phi)-8r\sin\theta(D_{11}r\cos\phi+\hat{D}_{11}r\sin\phi\\&+3D_{22}\sin\theta\cos2\phi))+2D_{02}r^2+12\sin2\phi\left(\cos2\theta\left(\hat{D}_{22}r^2+4\hat{E}_{12}\mu+5\hat{E}_{22}\mu\right)\right.\\&\left.-\hat{D}_{22}r^2+4\hat{E}_{12}\mu+3\hat{E}_{22}\mu\right)\Big\}.\end{aligned}\tag{C8}$$

The unknown coefficients $D_{mn}, \hat{D}_{mn}, E_{mn}, \hat{E}_{mn}, F_{mn}, \hat{F}_{mn}$ are obtained by satisfying the boundary condition given by (3.3) and are provided in tables 1 and 2. The coefficients $\triangledown$, ∇^*, $\triangle$, $\triangle^*$ in table 1 are given by

$$\triangledown=-\mu a\bar{U}_p\left(\frac{2a^2}{5}+\Gamma\right)+\frac{2}{a^2}\mu E_{01},\tag{C9}$$

$$\nabla^*=\mu a\left[U_s-\bar{U}_p\left(\frac{2a^2}{5}+\Gamma\right)\right]+\frac{2}{a^2}\mu E_{01},\tag{C10}$$

$$\triangle=B_{01}-\frac{a^3}{2}\bar{U}_p\left(\frac{3a^2}{5}+\frac{\Gamma}{2}\right),\quad \triangle^*=\frac{a^3}{4}U_s+B_{01}-\frac{a^3}{2}\bar{U}_p\left(\frac{3a^2}{5}+\frac{\Gamma}{2}\right).\tag{C11a,b}$$

The translational and rotational velocities are obtained from the force- and torque-free conditions along each direction. Specifically, in spherical coordinates, the force- and

Coefficients	$\boldsymbol{e}_x$	$\boldsymbol{e}_y$	$\boldsymbol{e}_z$
D_{11}	$\frac{\mu}{a^2}(-a^3 U_s + 2E_{11})$	$\frac{2\mu}{a^2}E_{11}$	$\frac{2\mu}{a^2}E_{11}$
D_{12}	$\mu\left(-\frac{2a^3\dot{\gamma}_1}{3}\bar{U}_p + \frac{6}{a^2}E_{12}\right)$	–	–
$\hat{D}_{11}$	$\frac{2\mu}{a^2}\hat{E}_{11}$	$\frac{\mu}{a^2}(-a^3 U_s + 2\hat{E}_{11})$	$\frac{2\mu}{a^2}\hat{E}_{11}$
$\hat{D}_{12}$	$\mu\left(-\frac{2a^3\dot{\gamma}_2}{3}\bar{U}_p + \frac{6}{a^2}\hat{E}_{12}\right)$	–	–
E_{11}	$-\frac{a^3}{4}U_s + B_{11}$	B_{11}	B_{11}
E_{12}	B_{12}	–	–
$\hat{E}_{11}$	$\hat{B}_{11}$	$-\frac{a^3}{4}U_s + \hat{B}_{11}$	$\hat{B}_{11}$
$\hat{E}_{12}$	$\hat{B}_{12}$	–	–
F_{11}	$-a^3\Omega_s + C_{11}$	C_{11}	C_{11}
F_{12}	C_{12}	–	–
$\hat{F}_{11}$	$\hat{C}_{11}$	$-a^3\Omega_s + \hat{C}_{11}$	$\hat{C}_{11}$
$\hat{F}_{12}$	$\hat{C}_{12}$	–	–

Table 2. Coefficients of the flow field for $m = 1$. The $-$ denotes a coefficient that remains the same across directions.

torque-free conditions in the $\boldsymbol{e}_x$ direction are

$$\int_0^{2\pi}\int_0^{\pi}\left(\sigma_{rr}\sin\theta\cos\phi + \sigma_{\theta r}\cos\theta\cos\phi - \sigma_{\phi r}\sin\phi\right)\big|_{r=a}\, a^2\sin\theta\,\mathrm{d}\theta\,\mathrm{d}\phi = 0, \tag{C12}$$

$$-\int_0^{2\pi}\int_0^{\pi}\left(\sigma_{\phi r}\cos\theta\cos\phi + \sigma_{\theta r}\sin\phi\right)\big|_{r=a}\, a^3\sin\theta\,\mathrm{d}\theta\,\mathrm{d}\phi = 0, \tag{C13}$$

the force- and torque-free conditions in the $\boldsymbol{e}_y$ direction are

$$\int_0^{2\pi}\int_0^{\pi}\left(\sigma_{rr}\sin\theta\sin\phi + \sigma_{\theta r}\cos\theta\sin\phi + \sigma_{\phi r}\cos\phi\right)\big|_{r=a}\, a^2\sin\theta\,\mathrm{d}\theta\,\mathrm{d}\phi = 0, \tag{C14}$$

$$-\int_0^{2\pi}\int_0^{\pi}\left(\sigma_{\phi r}\cos\theta\sin\phi - \sigma_{\theta r}\cos\phi\right)\big|_{r=a}\, a^3\sin\theta\,\mathrm{d}\theta\,\mathrm{d}\phi = 0, \tag{C15}$$

and the force- and torque-free conditions in the $\boldsymbol{e}_z$ direction are

$$\int_0^{2\pi}\int_0^{\pi}(\sigma_{rr}\cos\theta - \sigma_{\theta r}\sin\theta)|_{r=a}\, a^2\sin\theta\,\mathrm{d}\theta\,\mathrm{d}\phi = 0, \tag{C16}$$

$$\int_0^{2\pi}\int_0^{\pi}\sigma_{\phi r}\sin\theta\big|_{r=a}\, a^3\sin\theta\,\mathrm{d}\theta\,\mathrm{d}\phi = 0. \tag{C17}$$

References

Abadi, M., *et al.* 2015 TensorFlow: large-scale machine learning on heterogeneous systems. Software available from tensorflow.org.

ACEMOGLU, A. & YESILYURT, S. 2015 Effects of Poiseuille flows on swimming of magnetic helical robots in circular channels. *Microfluid Nanofluid* **19**, 1109–1122.

AGARWAL, D. & BIROS, G. 2020 Stable shapes of three-dimensional vesicles in unconfined and confined Poiseuille flow. *Phys. Rev. Fluids* **5**, 013603.

ASMOLOV, E.S. 1999 The inertial lift on a spherical particle in a plane Poiseuille flow at large channel Reynolds number. *J. Fluid Mech.* **381**, 63–87.

BLAKE, J.R. 1971 A spherical envelope approach to ciliary propulsion. *J. Fluid Mech.* **46**, 199–208.

CHISHOLM, N.G., LEGENDRE, D., LAUGA, E. & KHAIR, A.S. 2016 A squirmer across Reynolds numbers. *J. Fluid Mech.* **796**, 233–256.

CHOUDHARY, A., PAUL, S., RUHLE, F. & STARK, H. 2022 How inertial lift affects the dynamics of a microswimmer in Poiseuille flow. *Commun. Phys.* **5**, 14.

CHWANG, A.T. & WU, T.Y.-T. 1975 Hydromechanics of low-Reynolds-number flow. Part 2. Singularity methods for Stokes flows. *J. Fluid Mech.* **67**, 787–815.

DANKER, G., VLAHOVSKA, P.M. & MISBAH, C. 2009 Vesicles in Poiseuille flow. *Phys. Rev. Lett.* **102**, 148102.

DATT, C., ZHU, L., ELFRING, G.J. & PAK, O.S. 2015 Squirming through shear-thinning fluids. *J. Fluid Mech.* **784**, R1.

DENISSENKO, P., KANTSLER, V., SMITH, D.J. & KIRKMAN-BROWN, J. 2012 Human spermatozoa migration in microchannels reveals boundary-following navigation. *Proc. Natl Acad. Sci. USA* **21**, 8007–8010.

DRESCHER, K., DUNKEL, J., CISNEROS, L.H., GANGULY, S. & GOLDSTEIN, R.E. 2011 Fluid dynamics and noise in bacterial cell-cell and cell-surface scattering. *Proc. Natl Acad. Sci. USA* **108**, 10940–10945.

DRESCHER, K., LEPTOS, K.C., TUVAL, I., ISHIKAWA, T., PEDLEY, T.J. & GOLDSTEIN, R.E. 2009 Dancing *Volvox*: hydrodynamic bound states of swimming algae. *Phys. Rev. Lett.* **102**, 168101.

EVANS, A.A., ISHIKAWA, T., YAMAGUCHI, T. & LAUGA, E. 2011 Orientational order in concentrated suspensions of spherical microswimmers. *Phys. Fluids* **23**, 111702.

GAO, W., KAGAN, D., PAK, O.S., CLAWSON, C., CAMPUZANO, S., CHULUUN-ERDENE, E., Fullerton, E., Zhang, L., Lauga, E. & Wang, J. 2012 Cargo-towing fuel-free magnetic nanoswimmers for targeted drug delivery. *Small* **8**, 460–467.

GILPIN, W., PRAKASH, V.N. & PRAKASH, M. 2017 Vortex arrays and ciliary tangles underlie the feeding-swimming trade-off in starfish larvae. *Nat. Phys.* **13**, 380–386.

GOLDSMITH, H.L. & MASON, S.G. 1961 Axial migration of particles in Poiseuille flow. *Nature* **190**, 1095–1096.

HANNA, J.A. & VLAHOVSKA, P.M. 2010 Surfactant-induced migration of a spherical drop in Stokes flow. *Phys. Fluids* **22**, 013102.

HAPPEL, J. & BRENNER, H. 1973 *Low Reynolds Number Hydrodynamics: with Special Applications to Particulate Media*. Noordhoff International Publishing.

HOOD, K., LEE, S. & ROPER, M. 2015 Inertial migration of a rigid sphere in three-dimensional Poiseuille flow. *J. Fluid Mech.* **765**, 452–479.

ISHIKAWA, T., KAJIKI, S., IMAI, Y. & OMORI, T. 2016 Nutrient uptake in a suspension of squirmers. *J. Fluid Mech.* **789**, 481–499.

JABBARZADEH, M. & FU, H.C. 2018 Viscous constraints on microorganism approach and interaction. *J. Fluid Mech.* **851**, 715–738.

JEONG, J.-T. 2019 Axisymmetric Stokes flow around a sphere translating along the axis of a circular cylinder. *Eur. J. Mech. (*B*/Fluids)* **77**, 252–258.

KESSLER, J.O. 1985 Hydrodynamic focusing of motile algal cells. *Nature* **313**, 218.

LAMB, H. 1945 *Hydrodynamics*. Cambridge University Press.

LESHANSKY, A.M. 2009 Enhanced low-Reynolds-number propulsion in heterogeneous viscous environments. *Phys. Rev.* E **80**, 051911.

LI, G., LAUGA, E. & ARDEKANI, A.M. 2021 Microswimming in viscoelastic fluids. *J. Non-Newtonian Fluid Mech.* **297**, 104655.

LI, J., DE AVILA, B.E.-F., GAO, W., ZHANG, L. & WANG, J. 2017 Micro/nanorobots for biomedicine: delivery, surgery, sensing, and detoxification. *Sci. Robot.* **2**, eaam6431.

LIGHTHILL, M.J. 1952 On the squirming motion of nearly spherical deformable bodies through liquids at very small Reynolds number. *Comm. Pure Appl. Maths* **109**, 118.

LU, L., MENG, X., MAO, Z. & KARNIADAKIS, G.E. 2021 DeepXDE: a deep learning library for solving differential equations. *SIAM Rev.* **63**, 208–228.

MAGAR, V., GOTO, T. & PEDLEY, T.J. 2003 Nutrient uptake by a self-propelled steady squirmer. *Q. J. Mech. Appl. Maths* **56**, 65–91.

MARUMO, A., YAMAGISHI, M. & YAJIMA, J. 2021 Three-dimensional tracking of the ciliate Tetrahymena reveals the mechanism of ciliary stroke-driven helical swimming. *Commun. Biol.* **4**, 1209.

MIURA, T., OOSAWA, H., SAKAI, M., SYUNDOU, Y., BAN, T. & SHIOI, A. 2010 Autonomous motion of vesicle via ion exchange. *Langmuir* **26**, 1610–11618.

NELSON, B.J., KALIAKATSOS, I.K. & ABBOTT, J.J. 2010 Microrobots for minimally invasive medicine. *Annu. Rev. Biomed. Engng* **12**, 55–85.

NGANGUIA, H. & PAK, O.S. 2018 Squirming motion in a Brinkman medium. *J. Fluid Mech.* **855**, 554–573.

OMORI, T., KIKUCHI, K., SCHMITZ, M., PAVLOVIC, M., CHUANG, C.-H. & ISHIKAWA, T. 2022 Rheotaxis and migration of an unsteady microswimmer. *J. Fluid Mech.* **930**, A30.

OUYANG, Z., LIN, Z., LIN, J., YU, Z. & PHAN-THIEN, N. 2023 Cargo carrying with an inertial squirmer in a Newtonian fluid. *J. Fluid Mech.* **959**, A25.

PAK, O.S., FENG, J. & STONE, H. 2014 Viscous Marangoni migration of a drop in a Poiseuille flow at low surface Péclet numbers. *J. Fluid Mech.* **753**, 535–552.

PAK, O.S. & LAUGA, E. 2014 Generalized squirming motion of a sphere. *J. Engng Maths* **88**, 1–28.

PAK, O.S., ZHU, L., BRANDT, L. & LAUGA, E. 2012 Micropropulsion and microrheology in complex fluids via symmetry breaking. *Phys. Fluids* **24**, 103102.

PALANIAPPAN, D. & DARIPA, P. 2000 Compound droplet in extensional and paraboloidal flows. *Phys. Fluids* **12**, 2377–2385.

PALANIAPPAN, D. & DARIPA, P. 2005 On axisymmetric creeping flows involving a hybrid droplet. *Physica* A **346**, 217–249.

PEDLEY, T.J. 2016 Spherical squirmers: models for swimming micro-organisms. *IMA J. Appl. Maths* **81**, 488.

PEDLEY, T.J. & KESSLER, J.O. 1990 A new continuum model for suspensions of gyrotactic micro-organisms. *J. Fluid Mech.* **212**, 155.

PIETRZYK, K., NGANGUIA, H., DATT, C., ZHU, L., ELFRING, G.J. & PAK, O.S. 2019 Flow around a squirmer in a shear-thinning fluid. *J. Non-Newtonian Fluid Mech.* **268**, 101–110.

PODDAR, A., BANDOPADHYAY, A. & CHAKRABORTY, S. 2020 Near-wall hydrodynamic slip triggers swimming state transition of micro-organisms. *J. Fluid Mech.* **894**, A11.

REIGH, S.Y. & LAUGA, E. 2017 Two-fluid model for locomotion under self-confinement. *Phys. Rev. Fluids* **2**, 093101.

REIGH, S.Y., ZHU, L., GALLAIRE, F. & LAUGA, E. 2017 Swimming with a cage: low-Reynolds-number locomotion inside a droplet. *Soft Matt.* **13**, 3161.

RIFFELL, J.A. & ZIMMER, R.K. 2007 Sex and flow: the consequences of fluid shear for sperm-egg interactions. *J. Expl Biol.* **210**, 3644–3660.

RODRIGUES, M.F.V., LISICKI, M. & LAUGA, E. 2021 The bank of swimming organisms at the micron scale (BOSO-Micro). *PLoS ONE* **16**, e0252291.

RUTLLANT, J., LOPEZ-BEJAR, M. & LOPEZ-GATIUS, F. 2005 Ultrastructural and rheological properties of bovine vaginal fluid and its relation to sperm motility fertilization: a review. *Reprod. Dom. Anim.* **40**, 79–86.

SCHONBERG, J.A. & HINCH, E.J. 1989 Inertial migration of a sphere in Poiseuille flow. *J. Fluid Mech.* **203**, 517–524.

SEGRÉ, G. & SILBERBERG, A. 1961 Radial particle displacements in Poiseuille flow of suspensions. *Nature* **189**, 209–210.

SHORT, M.B., SOLARI, C.A., GANGULY, S., POWERS, T.R., KESSLER, J.O. & GOLDSTEIN, R.E. 2006 Flows driven by flagella of multicellular organisms enhance long-range molecular transport. *Proc. Natl Acad. Sci. USA* **103**, 8315–8319.

THERY, A., MAAB, C.C. & LAUGA, E. 2023 Hydrodynamic interactions between squirmers near walls: far-field dynamics and near-field cluster stability. *R. Soc. Open Sci.* **10**, 230223.

THUTUPALLI, S., SEEMANN, R. & HERMINGHAUS, S. 2011 Swarming behavior of simple model squirmers. *New J. Phys.* **13**, 073021.

TSANG, A.C.H., DEMIR, E., DING, Y. & PAK, O.S. 2020 Roads to smart artificial microswimmers. *Adv. Intell. Syst.* **2**, 1900137.

UPPALURI, S., HEDDERGOTT, N., STELLAMANNS, E., HERMINGHAUS, S., ZOTTL, A., STARK, H., ENGSTLER, M. & PFOHL, T. 2012 Flow loading induces oscillatory trajectories in a bloodstream parasite. *Biophys. J.* **103**, 1162–1169.

WALKER, B.J., ISHIMOTO, K., MOREAU, C., GAFFNEY, E.A. & DALWADI, M.P. 2022 Emergent rheotaxis of shape-changing swimmers in Poiseuille flow. *J. Fluid Mech.* **944**, R2.

WANG, J., *et al.* 2022 Volbots: volvox microalgae-based robots for multimode precision imaging and therapy. *Adv. Funct. Mater.* **32**, 2201800.

WU, Z., CHEN, Y., MUKASA, D., PAK, O.S. & GAO, W. 2020 Medical micro/nanorobots in complex media. *Chem. Soc. Rev.* **49**, 8088–8112.

ZHANG, H., LI, Z., GAO, C., FAN, X., PANG, Y., LI, T., WU, Z., XIE, H. & HE, Q. 2021 Dual-responsive biohybrid neutrobots for active target delivery. *Sci. Robot.* **6**, eaaz9519.

ZHU, L., LAUGA, E. & BRANDT, L. 2012 Self-propulsion in viscoelastic fluids: pushers vs pullers. *Phys. Fluids* **24**, 051902.

ZIMMER, R.K. & RIFFELL, J.A. 2011 Sperm chemotaxis, fluid shear, and the evolution of sexual reproduction. *Proc. Natl Acad. Sci. USA* **108**, 13200–13205.

ZOTTL, A. & STARK, H. 2012 Nonlinear dynamics of a microswimmer in Poiseuille flow. *Phys. Rev. Lett.* **108**, 218104.